Channels for streaming instability in dusty discs

Etienne Jaupart, Guillaume Laibe

Monthly Notices
of the
ROYAL ASTRONOMICAL SOCIETY

MNRAS **492,** 4591–4598 (2020)
Advance Access publication 2020 January 9

doi:10.1093/mnras/staa057

Channels for streaming instability in dusty discs

Etienne Jaupart★ and Guillaume Laibe

Univ Lyon, Univ Lyon1, Ens de Lyon, CNRS, Centre de Recherche Astrophysique de Lyon UMR5574, F-69230 Saint-Genis-Laval, France

Accepted 2020 January 7. Received 2020 January 6; in original form 2019 November 5

ABSTRACT

Streaming instability is a privileged channel to bridge the gap between collisional growth of dust grains and planetesimal formation triggered by gravity. This instability is thought to develop through its secular mode, which is long-time growing and may not develop easily in real discs. We address this point by revisiting its perturbation analysis. A third-order expansion with respect to the Stokes number reveals important features overlooked so far. The secular mode can be stable. Epicycles can be unstable, more resistant to viscosity, and are identified by Green's function analysis as promising channels for planetesimals formation.

Key words: instabilities – planets and satellites: formation – protoplanetary discs.

1 INTRODUCTION

Spatially resolved observations have revealed the presence of substructures in discs around young stars (e.g. van der Marel et al. 2013; ALMA Partnership 2015; Benisty et al. 2015; Andrews et al. 2018; Avenhaus et al. 2018). Whether these structures are created by planets or not is still a matter of ardent discussions. Recent direct imaging of massive planets inside the disc around PDS 70 (Keppler et al. 2018; Christiaens et al. 2019; Keppler et al. 2019), or analysis of gas kinematics (Pinte et al. 2018; Teague et al. 2018; Pinte et al. 2019) suggest that at least some of these structures are indeed created by young planets. This raises the question of forming these objects in less than a typical million years. This leaves a critically short time for the solid material arising from the dusty interstellar medium to grow over ∼30 orders of magnitude in mass (Chiang & Youdin 2010; Testi et al. 2014). Hit and stick collisions form millimetre pebbles relatively easily, but becomes inefficient to overcome the metre-size barrier (e.g. Blum & Wurm 2008). It has therefore been proposed that dust particles should concentrate through hydrodynamical processes in dust-rich clouds, up to the stage where gravity takes over and forms planetesimals. Proceeding to this concentration is best explained by the so-called streaming instability, which has been discovered by Youdin & Goodman (2005) following an idea of Goodman & Pindor (2000). In thin cold discs, dust and gas exchange angular momentum through drag and drift radially with respect to each other. However, interactions between these two streams can destabilize the flows for small perturbations. Gas is then expelled in the vertical direction, leading to a local enrichment in dust (Youdin & Goodman 2005; Youdin & Johansen 2007; Jacquet, Balbus & Latter 2011). This behaviour is generic to a more general class of instability called resonant drag instabilities (e.g. Hopkins & Squire 2018; Squire & Hopkins 2018; Zhuravlev V. V. 2019). Numerical simulations have shown that when reaching the non-linear stage, streaming instability gives rise to very high local solid concentration (e.g. Johansen et al. 2007; Johansen & Youdin 2007; Balsara et al. 2009; Johansen, Youdin & Mac Low 2009; Bai & Stone 2010a,b,c; Tilley et al. 2010; Johansen, Youdin & Lithwick 2012; Kowalik et al. 2013; Lyra & Kuchner 2013) and as such is one of the corner stones of planet formation (e.g. Drążkowska & Dullemond 2014; Yang & Johansen 2014; Simon et al. 2016; Carrera et al. 2017; Schäfer, Yang & Johansen 2017; Schoonenberg & Ormel 2017).

So far, the instability has been mostly thought to develop through its secular mode. However, this mode has been found to grow slowly, raising concerns regarding the ability of the instability to occur in real discs. In particular, streaming instability is not thought to resist viscous damping even in moderately viscous discs ($\alpha \gtrsim 10^{-5} - 10^{-4}$, Youdin & Goodman 2005), except maybe in local pressure maxima (Auffinger & Laibe 2018). Streaming instability may also be quenched when the dust distribution is not monodisperse (Krapp et al. 2019). Hence, the necessity of looking for possible alternative channels. One possibility is the so-called settling instability that may develop faster (Squire & Hopkins 2018). Another possibility has actually been suggested in the original article of Youdin & Goodman (2005). They note that epicycles can become unstable but did not quantify the conditions under which this occurs. Since alternative unstable modes have not attracted much interest so far, we investigate the possible existence of complementary channels to concentrate dust. Such a mode should have a growth rate that competes with the secular mode, resists viscous damping, and be favourably excited in real discs. To identify it, we revisit the perturbation analysis by obtaining an excellent approximation of the dispersion relation that factorizes the epicycles and the secular mode. This study is hence organized as follows: the linear set of equations governing the evolution of a small local perturbation inside the dusty disc is presented in Section 2. The analytic study of the unstable modes is performed and stability conditions are derived in Section 3. In Section 4, we discuss the resilience against viscous damping and characterize the development of the streaming instability in real discs by the mean of Green's function analysis.

★ E-mail: ejaupart@gmail.com

2 EQUATIONS OF MOTION

2.1 Mass and momentum conservation

We consider a non-magnetic non-self-graviting vertically isothermal inviscid and unstratified disc orbiting a point-like central star. Dust grains are modelled by compact homogeneous spheres. Dust is treated as a continuous pressureless and inviscid phase (Saffman 1962). We neglect grain growth and fragmentation. Dust and gas exchange momentum via a drag term, whose characteristic time is called the stopping time $t_{\rm stop}$. Mass and momentum conservation for gas and dust are given in the usual cylindrical coordinates by

$$\frac{\partial \rho_{\rm g}}{\partial t} + \boldsymbol{\nabla} \cdot \left(\rho_{\rm g} \boldsymbol{V}_{\rm g} \right) = 0, \tag{1}$$

$$\frac{\partial \rho_{\rm p}}{\partial t} + \boldsymbol{\nabla} \cdot \left(\rho_{\rm p} \boldsymbol{V}_{\rm p} \right) = 0, \tag{2}$$

$$\frac{\partial \boldsymbol{V}_{\rm g}}{\partial t} + \left(\boldsymbol{V}_{\rm g} \cdot \boldsymbol{\nabla} \right) \boldsymbol{V}_{\rm g} = -\Omega_{\rm K}^2 \boldsymbol{r} - \frac{1}{\rho_{\rm g}} \boldsymbol{\nabla} P + \frac{\rho_{\rm p}}{\rho_{\rm g}} \frac{\boldsymbol{V}_{\rm p} - \boldsymbol{V}_{\rm g}}{t_{\rm stop}}, \tag{3}$$

$$\frac{\partial \boldsymbol{V}_{\rm p}}{\partial t} + \left(\boldsymbol{V}_{\rm p} \cdot \boldsymbol{\nabla} \right) \boldsymbol{V}_{\rm p} = -\Omega_{\rm K}^2 \boldsymbol{r} - \frac{\boldsymbol{V}_{\rm p} - \boldsymbol{V}_{\rm g}}{t_{\rm stop}}, \tag{4}$$

where $\rho_{\rm g}$ and $\rho_{\rm p}$ denote the gas and the dust densities, $\boldsymbol{V}_{\rm g}$ and $\boldsymbol{V}_{\rm p}$ denote the gas and dust velocities, $\Omega_{\rm K}$ is the orbital frequency at a given distance r, and P is the pressure of the gas. The notations of Youdin & Goodman (2005) are adopted for sake of clarity. This system of equations can be either closed with an equation of state or an incompressibility condition for the gas (Boussinesq approximation).

We follow Youdin & Goodman (2005) and Jacquet et al. (2011) by adopting a single fluid description of the dust/gas for performing the linear stability analysis. We introduce the total density $\rho = \rho_{\rm g} + \rho_{\rm p}$ and the centre-of-mass velocity $\rho \boldsymbol{V} = \rho_{\rm g} \boldsymbol{V}_{\rm g} + \rho_{\rm p} \boldsymbol{V}_{\rm p}$. The differential dynamics of the mixture is then unambiguously described in terms of the drift velocity $\Delta \boldsymbol{V} = \boldsymbol{V}_{\rm p} - \boldsymbol{V}_{\rm g}$ and the mass fractions $f_{\rm p,\,g} = \rho_{\rm p,\,g}/\rho$ (e.g. Laibe & Price 2014; Lebreuilly, Commerçon & Laibe 2019). Similarly to Youdin & Goodman (2005), we close the system of equations with an incompressibility condition for practical tractability. Finally, we write the equations of motion in the frame rotating at frequency $\boldsymbol{\Omega}_{\rm K,0} \equiv \boldsymbol{\Omega}_{\rm K}(r_0)$ where r_0 is an arbitrary radius of interest. Under these assumptions, equations (1)–(4) reduce to

$$\frac{\partial \rho}{\partial t} + \boldsymbol{\nabla} \cdot (\rho \boldsymbol{V}) = 0, \tag{5}$$

$$\boldsymbol{\nabla} \cdot \left(\boldsymbol{V} - f_{\rm p} \Delta \boldsymbol{V} \right) = 0, \tag{6}$$

$$\frac{{\rm d}\boldsymbol{V}}{{\rm d}t} = -2\boldsymbol{\Omega}_{\rm K,0} \times \boldsymbol{V} + \left(\Omega_{\rm K,0}^2 - \Omega_{\rm K}^2 \right) \boldsymbol{r} - \frac{\boldsymbol{\nabla} P}{\rho} + \boldsymbol{F}\left(\rho, f_{\rm p}, \Delta \boldsymbol{V} \right), \tag{7}$$

$$\frac{{\rm d}\Delta \boldsymbol{V}}{{\rm d}t} = -\frac{\Delta \boldsymbol{V}}{f_{\rm g} t_{\rm stop}} + \frac{\boldsymbol{\nabla} \boldsymbol{P}}{f_{\rm g} \rho} - (\Delta \boldsymbol{V} \cdot \boldsymbol{\nabla}) \boldsymbol{V} + \boldsymbol{G}\left(f_{\rm p}, \Delta \boldsymbol{V} \right), \tag{8}$$

where

$$\frac{\rm d}{{\rm d}t} = \frac{\partial}{\partial t} + (\boldsymbol{V} \cdot \boldsymbol{\nabla}), \tag{9}$$

$$\boldsymbol{F}\left(\rho, f_{\rm p}, \Delta \boldsymbol{V} \right) = -\frac{1}{\rho} \boldsymbol{\nabla} \cdot \left(f_{\rm p} \left(1 - f_{\rm p} \right) \rho \Delta \boldsymbol{V} \otimes \Delta \boldsymbol{V} \right), \tag{10}$$

$$\boldsymbol{G}\left(f_{\rm p}, \Delta \boldsymbol{V} \right) = f_{\rm p} (\Delta \boldsymbol{V} \cdot \boldsymbol{\nabla}) \left(f_{\rm p} \Delta \boldsymbol{V} \right) - f_{\rm g} (\Delta \boldsymbol{V} \cdot \boldsymbol{\nabla}) \left(f_{\rm g} \Delta \boldsymbol{V} \right). \tag{11}$$

The incompressibility condition (6) reduces to ${\rm d}\rho = {\rm d}\rho_{\rm p}$, relating directly the dust overconcentration sought for to a local increase of the total density. This implies that gas cannot accumulate locally.

2.2 Local perturbations in a shearing box

2.2.1 Steady state solutions

We use a Cartesian shearing-box approximation $(\hat{\boldsymbol{x}}, \hat{\boldsymbol{y}}, \hat{\boldsymbol{z}})$ (Goldreich & Lynden-Bell 1965) and limit the study to local perturbations. Under this approximation, gas pressure can be decomposed into a background component, which consists of a small constant pressure force $g_{\rm e}$ and an additional perturbation. Denoting H the pressure scale height of the gas, we have

$$g_{\rm e} \equiv -\frac{1}{\rho} \left. \frac{\partial P}{\partial r} \right|_{r_0} \sim \left(\frac{H}{r_0} \right)^2 \Omega_{\rm K,0}^2 \, r_0 > 0, \tag{12}$$

since the disc is warmer and denser close to the star. The steady-state solution of equations (5)–(8) has been found by Nakagawa, Sekiya & Hayashi (1986)

$$\boldsymbol{V}_0 = \left(-\frac{3}{2} \Omega_{\rm K,0} x - \frac{g_{\rm e}}{2\Omega_{\rm K,0}} \right) \hat{\boldsymbol{y}}, \tag{13}$$

$$\Delta \boldsymbol{V}_0 = -\frac{g_{\rm e} t_{\rm stop}}{1 + S_{\rm t}^2} \hat{\boldsymbol{x}} + \frac{f_{\rm g} g_{\rm e} \Omega_{\rm K,0} t_{\rm stop}^2}{2\left(1 + S_{\rm t}^2 \right)} \hat{\boldsymbol{y}}. \tag{14}$$

To ease the forthcoming derivations, we adopt a definition of the Stokes number $S_{\rm t} \equiv f_{\rm g} \Omega_K t_{\rm stop}$ that slightly differs from the usual notation by a factor $f_{\rm g}$. Equations (13)–(14) express that the motion is overall sub-Keplerian and that grains drift inwards towards high pressure regions, pushing gas outwards by angular momentum conservation. The drift velocity is the largest for Stokes numbers of order unity.

2.2.2 Dimensionless quantities

The natural time-scale of the problem is the orbital time-scale $\tau_0 \equiv \Omega_{\rm K,0}^{-1}$. The physical length $\lambda_{\rm e}$ of the steady state described in Section 2.2.1 is therefore $\lambda_{\rm e} \equiv g_{\rm e}/\Omega_{\rm K,0}^2 \sim (H/r_0)\, H \ll H$. $\lambda_{\rm e}$ gives the order of magnitude of the relative distance over which dust grains with $S_{\rm t} \sim 1$ and gas drift relatively to each other in a time τ_0. Hence, we introduce the dimensionless time τ, positions (χ, ζ), and velocity $\boldsymbol{U}$ defined by

$$t \equiv \tau_0 \tau, \tag{15}$$

$$(x, z) \equiv \lambda_{\rm e} (\chi, \zeta), \tag{16}$$

$$\boldsymbol{V} \equiv \frac{\lambda_{\rm e}}{\tau_0} \boldsymbol{U}, \tag{17}$$

such as

$$\boldsymbol{U}_0 = -\left(\frac{3}{2} \chi + \frac{1}{2} \right) \hat{\boldsymbol{y}}, \tag{18}$$

$$\Delta \boldsymbol{U}_0 = -\left(\frac{S_{\rm t}}{f_{\rm g}\left(1 + S_{\rm t}^2 \right)} \hat{\boldsymbol{x}} - \frac{S_{\rm t}^2}{2 f_{\rm g}\left(1 + S_{\rm t}^2 \right)} \hat{\boldsymbol{y}} \right). \tag{19}$$

2.2.3 *Linear stability analysis*

We perform a linear perturbation analysis of equations (18) and (19), assuming a perturbation of the form

$$\boldsymbol{U} = \boldsymbol{U}_0 + \boldsymbol{u}(\tau, \chi, \zeta), \tag{20}$$

$$\Delta\boldsymbol{U} = \Delta\boldsymbol{U}_0 + \Delta\boldsymbol{u}(\tau, \chi, \zeta), \tag{21}$$

$$\frac{\rho}{\rho_0} = 1 + \delta(\tau, \chi, \zeta), \tag{22}$$

$$\frac{P - P_0}{\rho_0 g_e \lambda_e} = -\chi + h(\tau, \chi, \zeta), \tag{23}$$

where P_0 denotes the pressure of the gas at the centre of the box. Following Youdin & Goodman (2005) and Jacquet et al. (2011), the perturbation f is decomposed under axisymmetric Fourier modes of the form

$$f(\tau, \chi, \zeta) = \tilde{f} \mathrm{e}^{\mathrm{i}(\kappa_x \chi + \kappa_z \zeta - \omega\tau)}. \tag{24}$$

κ_x should satisfy $|\kappa_x| \gg (H/r_0)^2$ to ensure consistency with the shearing-box approximation, and κ_z should satisfy $|\kappa_z| \gg (H/r_0)$, to neglect the stratification of the disc. In practice, these conditions are not restrictive. The resulting set of equation in dimensionless form is

$$-\mathrm{i}\omega\tilde{\delta} + \mathrm{i}\boldsymbol{\kappa}\cdot\tilde{\boldsymbol{u}} = 0, \tag{25}$$

$$\boldsymbol{\kappa}\cdot\tilde{\boldsymbol{u}} - f_\mathrm{p}\boldsymbol{\kappa}\cdot\Delta\tilde{\boldsymbol{u}} + \kappa_x \frac{S_\mathrm{t}}{1+S_\mathrm{t}^2}\tilde{\delta} = 0, \tag{26}$$

$$-\mathrm{i}\omega\tilde{\boldsymbol{u}} - 2\tilde{u}_y\hat{\boldsymbol{x}} + \frac{1}{2}\tilde{u}_x\hat{\boldsymbol{y}} + \tilde{\delta}\hat{\boldsymbol{x}} + \mathrm{i}\boldsymbol{\kappa}\tilde{h} + \tilde{\boldsymbol{F}}' = 0, \tag{27}$$

$$-\mathrm{i}\omega\Delta\tilde{\boldsymbol{u}} - 2\Delta\tilde{u}_y\hat{\boldsymbol{x}} + \frac{1}{2}\Delta\tilde{u}_x\hat{\boldsymbol{y}} - \mathrm{i}\frac{\boldsymbol{\kappa}}{f_\mathrm{g}}\tilde{h} + \frac{\Delta\tilde{\boldsymbol{u}} + \tilde{\delta}\Delta\boldsymbol{U}_0}{S_\mathrm{t}} - \mathrm{i}\kappa_x\frac{S_\mathrm{t}}{f_\mathrm{g}\left(1+S_\mathrm{t}^2\right)}\tilde{\boldsymbol{u}} + \tilde{\boldsymbol{G}}' = 0, \tag{28}$$

where

$$\tilde{\boldsymbol{F}}' = \mathrm{i}f_\mathrm{g}\left\{\left(f_\mathrm{p}\boldsymbol{\kappa}\cdot\Delta\tilde{\boldsymbol{u}} - \kappa_x\frac{S_\mathrm{t}}{1+S_\mathrm{t}^2}\tilde{\delta}\right)\Delta\boldsymbol{U}_0 - \frac{f_\mathrm{p}\kappa_x S_\mathrm{t}}{f_\mathrm{g}\left(1+S_\mathrm{t}^2\right)}\Delta\tilde{\boldsymbol{u}}\right\}, \tag{29}$$

$$\tilde{\boldsymbol{G}}' = -\mathrm{i}\kappa_x\frac{S_\mathrm{t}}{f_\mathrm{g}\left(1+S_\mathrm{t}^2\right)}\left\{\left(2f_\mathrm{p}-1\right)\Delta\tilde{\boldsymbol{u}} - f_\mathrm{g}\Delta\boldsymbol{U}_0\tilde{\delta}\right\}. \tag{30}$$

Equations (25)–(30) define a linear system of eight equations on the eight physical quantities $\tilde{\delta}$, $\tilde{\boldsymbol{u}}$, $\tilde{h}$, and $\Delta\tilde{\boldsymbol{u}}$ expressed in the above-defined dimensionless quantities (Youdin & Goodman 2005). A lengthy dispersion relation is obtained by setting to zero the polynomial determinant $\mathcal{P}_8$ of the system (see Appendix A).

3 UNSTABLE MODES

3.1 Reduced system: linear expansion in S_t

Since the expression of $\mathcal{P}_8$ is cumbersome, Youdin & Goodman (2005) and Jacquet et al. (2011) study alternatively a simplified set of equations by expanding equations (25)–(30) to the first order with respect to the Stokes number. The key idea brought by Youdin & Goodman (2005) and Jacquet et al. (2011) is to use the so-called terminal velocity approximation. Values at steady state are used for the differential velocity between gas and dust for both the mean flow and the perturbation, assuming $S_\mathrm{t} \ll 1$ and performing the related Taylor expansion of the system. The resulting system is

$$-\mathrm{i}\omega\tilde{\delta} + \mathrm{i}\boldsymbol{\kappa}\cdot\tilde{\boldsymbol{u}} = 0, \tag{31}$$

$$\mathrm{i}\boldsymbol{\kappa}\cdot\tilde{\boldsymbol{u}} - \mathrm{i}\kappa_x S_\mathrm{t}\left(\frac{f_\mathrm{p}}{f_\mathrm{g}} - 1\right)\tilde{\delta} + f_\mathrm{p}\boldsymbol{\kappa}^2\frac{S_\mathrm{t}}{f_\mathrm{g}}\tilde{h} = 0, \tag{32}$$

$$-\mathrm{i}\omega\tilde{\boldsymbol{u}} - 2\tilde{u}_y\hat{\boldsymbol{x}} + \frac{1}{2}\tilde{u}_x\hat{\boldsymbol{y}} + \tilde{\delta}\hat{\boldsymbol{x}} + \mathrm{i}\boldsymbol{\kappa}\tilde{h} = 0, \tag{33}$$

$$\Delta\tilde{\boldsymbol{u}} = \mathrm{i}S_\mathrm{t}\frac{\tilde{h}\boldsymbol{\kappa}}{f_\mathrm{g}} + \frac{S_\mathrm{t}}{f_\mathrm{g}}\tilde{\delta}\hat{\boldsymbol{x}}. \tag{34}$$

One obtains the dispersion relation $P_\mathrm{Jac}(\omega) = 0$, with

$$P_\mathrm{Jac}(\omega) \equiv S_\mathrm{t}\varepsilon\omega^4 + \mathrm{i}\omega^3 + S_\mathrm{t}\left(\mathrm{i}\kappa_\mathrm{x} - \varepsilon\right)\omega^2 - \mathrm{i}\cos^2\theta\,\omega + \mathrm{i}\kappa_\mathrm{x}\cos^2\theta\left(\varepsilon - 1\right)S_\mathrm{t}, \tag{35}$$

where $\cos\theta \equiv \kappa_z/\|\boldsymbol{\kappa}\|$ and $\varepsilon \equiv f_\mathrm{p}/f_\mathrm{g}$. Roots of equation (35) contains the secular mode ω_s of the streaming instability

$$\omega_\mathrm{s} = \frac{\kappa_x\left(f_\mathrm{p} - f_\mathrm{g}\right)}{f_\mathrm{g}}S_\mathrm{t} + \mathrm{o}(S_\mathrm{t}), \tag{36}$$

where the leftover $\mathrm{o}(S_\mathrm{t})$ of the right-hand side of equation (36) contributes at this order to the imaginary part as

$$\Im\left(\omega_\mathrm{s}\right) = \Im\left(\mathrm{o}\left(S_\mathrm{t}\right)\right) = \left(\frac{\kappa_x^2}{f_\mathrm{g}^2}\frac{\left(f_\mathrm{p} - f_\mathrm{g}\right)^2}{\cos^2\theta}\varepsilon\right)S_\mathrm{t}^3 = \mathcal{O}\left(S_\mathrm{t}^3\right). \tag{37}$$

Hence, Youdin & Goodman (2005) and Jacquet et al. (2011) infer a secular mode that is always unstable. The growth of the secular mode is interpreted by the mean of this reduced systems, by an interplay between drift towards pressure maxima, geostrophic balance, and gas incompressibility. Youdin & Goodman (2005) also mention that epicycles are unstable as well when $\kappa_z \gg \kappa_x$.

Similarly to Debras et al. (2020) – Appendix B – we apply the argument theorem on the polynomial $\mathcal{P}_\mathrm{jac}$ to be more quantitative. We find that when $|\kappa_x| < S_\mathrm{t}\kappa_z^2\varepsilon$, $\mathcal{P}_\mathrm{jac}$ has two unstable roots, one corresponding to an approximated secular mode and the second one being a modified epicycle. This result *on the reduced system* is exact (we verified it numerically). However, this criterion is *incorrect* for describing the complete system of perturbed equations. Actually, numerical calculation of the roots of $\mathcal{P}_8$ shows that under the criterion derived above and for $\varepsilon < 1$, only the epicycle is unstable. Indeed, the reduced model is of order S_t and provides residuals of order S_t^3. This strongly suggests that an expansion of order S_t^3 is required to extract quantitatively the physics of the unstable modes of the streaming instability.

3.2 Reduced system: third-order expansion in S_t

3.2.1 *Dispersion relation*

We perform an expansion of the system equations (25)–(30) to the order S_t^3 and obtain an approximated dispersion relation $\mathcal{P}_8^{(3)}$. The detailed expression of $\mathcal{P}_8^{(3)}$ is lengthy and is given in Appendix B. The key idea is to rearrange the terms via the Euclidian division that enforces a functional form that factorizes the epicycles and the

secular mode

$$\frac{\mathcal{P}_8^{(3)}(\omega)}{\kappa^2} \equiv \left(\omega - \left\{\cos\theta + \alpha_1 S_\mathrm{t} + \alpha_2 S_\mathrm{t}^2 + \alpha_3 S_\mathrm{t}^3\right\}\right) \times \left(\omega - \left\{-\cos\theta + \alpha_1 S_\mathrm{t} - \alpha_2 S_\mathrm{t}^2 + \alpha_3 S_\mathrm{t}^3\right\}\right) \times \left(\mathrm{i}\frac{S_\mathrm{t}^3}{f_\mathrm{g}}\omega^4 - \frac{2+f_\mathrm{g}}{f_\mathrm{g}} S_\mathrm{t}^2\omega^3 + \beta_2\omega^2 + \beta_1\omega + \beta_0\right) + S_\mathrm{t}^4\mathcal{R}^{(3)}(\omega). \tag{38}$$

The residual $\mathcal{R}^{(3)}$ is a polynomial of degree 5 such that $S_\mathrm{t}^4\mathcal{R}^{(3)}(\omega)$ is of order S_t^4 when $\omega \lesssim 1$, and has therefore negligible contribution *per* construction. The coefficients $\alpha_{1,2,3}$ and $\beta_{0,1,2}$ are given in Appendix C. The conditions of validity for the aforesaid expansion are $\cos^2\theta \gg S_\mathrm{t}^2, \kappa_x^2 S_\mathrm{t} \lesssim 1$ and $\kappa_z S_\mathrm{t} \lesssim 1$.

We note that performing the same technique while restraining the expansion to the first order in S_t gives an approximate dispersion relation under the form

$$\mathrm{i}\frac{\mathcal{P}_8^{(1)}(\omega)}{\kappa^2} \equiv (1 - 3\mathrm{i}\omega S_\mathrm{t})\, P_\mathrm{Jac}(\omega) + S_\mathrm{t}^2\mathcal{R}^{(1)}(\omega) = 0, \tag{39}$$

with

$$\mathcal{R}^{(1)}(\omega) \equiv 3\left\{\mathrm{i}\varepsilon\omega^5 - (\mathrm{i}\varepsilon + \kappa_x)\,\omega^3 + \cos^2\theta\,(1-\varepsilon)\,\omega\right\}. \tag{40}$$

Equation (39) demonstrates that the expansion of Section 3.1 is actually a first-order expansion in S_t, although it was not mentioned explicitly in previous studies. Equation (39) shows that for a set of parameters that maximizes the growth rate, ω_s is of order S_t and the model presented in Section 3.1 is accurate. This is actually the choice of parameters chosen by Youdin & Goodman (2005), certainly adopted to highlight the efficiency of the instability. This choice of parameter may explain why stability of the secular mode has been overlooked so far. When ω_s is *not* of order S_t, equation (39) shows that a linear expansion fails to describe quantitatively the evolution of the perturbations.

3.2.2 *Secular mode*

Equation (38) provides directly the expression ω_s of the frequency of the secular mode at third order with respect to S_t as

$$\omega_\mathrm{s} = \frac{\kappa_x\left(f_\mathrm{p} - f_\mathrm{g}\right)}{f_\mathrm{g}} S_\mathrm{t} + \omega_\mathrm{s}^{(3)} S_\mathrm{t}^3 + \mathcal{O}\left(S_\mathrm{t}^4\right), \tag{41}$$

with

$$\Im(\omega_\mathrm{s}^{(3)}) = \frac{\kappa_x^2}{f_\mathrm{g}^2}\left(\frac{(f_\mathrm{p} - f_\mathrm{g})^2}{\cos^2\theta}\varepsilon + 3 f_\mathrm{p}\left(f_\mathrm{p} - f_\mathrm{g}\right)\right). \tag{42}$$

The imaginary part of $\omega_\mathrm{s}^{(3)}$ is now consistently expressed up to the order S_t^3. This correction differs from the one obtained by a linear expansion equation (37) by its last term. The extra contribution originates from the terms $(\Delta\boldsymbol{U}\cdot\nabla)\boldsymbol{u}$ that corresponds to the differential advection of the perturbations by the gas and the dust. In a linear approximation, the contribution of the backreaction to the mean flow is negligible at order S_t (Nakagawa et al. 1986). However, this correction becomes important at order S_t^3. Equation (42) shows effects of backreaction on to the drift are significant in the regime where the streaming instability develops and must be accounted for. When $\kappa_x \gg \kappa_z$, equation (42) reduces to the analysis of Youdin & Goodman (2005) and Jacquet et al. (2011).

Equation (42) shows that this correction is critical to understand the development of the secular mode of the streaming instability.

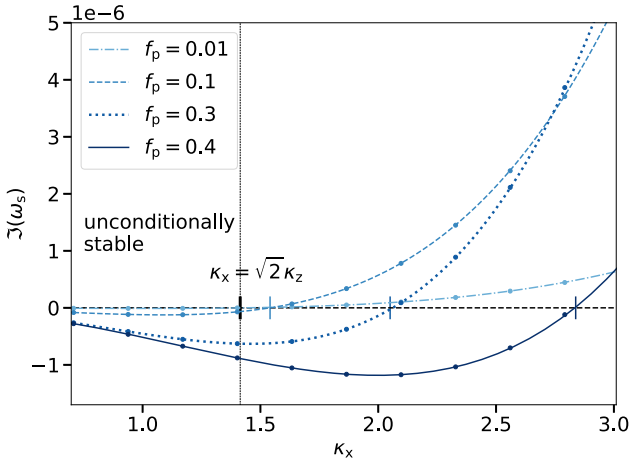

Figure 1. Imaginary part of the secular mode of the streaming instability calculated numerically from the full set of hydrodynamical equations $\mathcal{P}_8$ for dust fractions of $f_\mathrm{p} = 0.01, 0.1, 0.3, 0.4$ (from light to dark blue lines, respectively). The secular mode of the streaming instability is *always stable* when $f_\mathrm{p} < f_\mathrm{g}$ and $|\kappa_x| \leq \sqrt{2}|\kappa_z|$. Dots indicate the corresponding values predicted by the third-order expansion $\mathcal{P}_8^{(3)}$. The agreement is almost perfect. Here, the Stokes number is fixed to $S_\mathrm{t} = 0.01$ and $\kappa_z = 1$.

Indeed, the secular mode can be *stable* when the conditions

$$f_\mathrm{p} < f_\mathrm{g} \text{ and} \tag{43}$$

$$|\kappa_x| \leq \sqrt{2}|\kappa_z| \tag{44}$$

are satisfied. If not, the secular mode becomes unstable when

$$|\kappa_x| > |\kappa_z|\sqrt{\frac{2f_\mathrm{g} + f_\mathrm{p}}{f_\mathrm{g} - f_\mathrm{p}}} \geq \sqrt{2}|\kappa_z|, \tag{45}$$

with equality when $f_\mathrm{p} = 0$. If $f_\mathrm{p} > f_\mathrm{g}$, the secular mode is always unstable as evidenced by Youdin & Goodman (2005).

Fig. 1 illustrates this property by showing the imaginary part of ω_s obtained from a direct numerical resolution of the roots of the full dispersion relation $\mathcal{P}_8$. The roots obtained by the third-order expansion $\mathcal{P}_8^{(3)}$ are displayed as well, both of them showing almost perfect agreement. We fix $S_\mathrm{t} = 0.01$ to show that substantial corrections to the linear model can be obtained even for small grains. We then set $\kappa_z = 1$ and vary the dust fraction according from $f_\mathrm{p} = 0.01$ to $f_\mathrm{p} = 0.4$. When the criterion $|\kappa_x| \leq \sqrt{2}|\kappa_z|$ is satisfied, the imaginary part of ω_s is always negative and the secular mode is stable, as expected. For $|\kappa_x| > \sqrt{2}|\kappa_z|$, it becomes unstable when the condition of equation (45) is satisfied. The related critical values of $|\kappa_x|$ increase with f_p as predicted by equation (45).

3.2.3 *Unstable epicycles*

Equation (38) shows that epicycles can be unstable as well since

$$\Im(\omega_\mathrm{e}) = \frac{\varepsilon}{2} S_\mathrm{t}\left\{\frac{|\kappa_x|\varepsilon}{\cos\theta} S_\mathrm{t} - \kappa_x^2\left(1 + 3\varepsilon + \frac{(\varepsilon-1)^2}{\cos^2\theta}\right) S_\mathrm{t}^2 - \sin^2\theta \times \left(1 + \frac{|\kappa_x|(\varepsilon+2)}{2\cos\theta} S_\mathrm{t} + \left(\varepsilon(2\varepsilon+3)\sin^2\theta - (\varepsilon+1)^2\right) S_\mathrm{t}^2\right)\right\}. \tag{46}$$

The epicycle becomes therefore unstable under the necessary but unrestrictive condition $\sin^2\theta \ll 1$. A reasonable approximation for

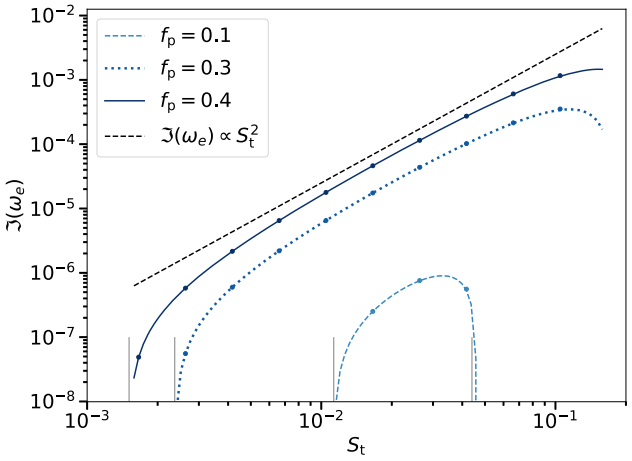

Figure 2. Imaginary part of the unstable epicycle of the streaming instability calculated numerically from the full set of hydrodynamical equations $\mathcal{P}_8$ for dust fractions of $f_p = 0.1$, 0.3, 0.4 (from light to dark blue lines, respectively) for varying Stokes numbers. The growth rates vary as S_t^2, as expected. Dots indicate the corresponding values predicted by the third-order expansion $\mathcal{P}_8^{(3)}$ and shows almost perfect agreement. The vertical solid grey lines indicate the analytic stability criterion given by equation (47). We choose $\kappa_x = 0.9$ and $\kappa_z = 30$ for the secular mode to be stable.

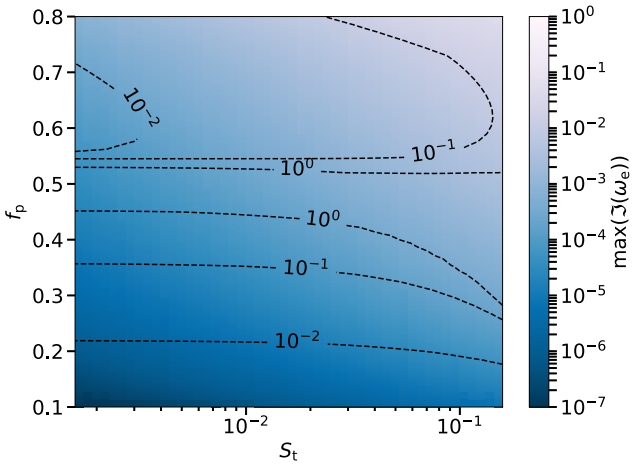

Figure 3. The maximum growth rate of the unstable epicycle, varying κ_x and κ_z within the range $\left[0.1; S_t^{-1}\right]$. Typical growth times of $\sim 10^3$ orbital periods are obtained for $f_p \gtrsim 0.2$ and $S_t \gtrsim 0.01$. Dashed black contours: ratio between the maximum growth rates of the epicycle versus the secular mode. These do not correspond to the same κ_x and κ_z a priori. The epicycle mode can grow as fast as the secular mode.

instability is derived by expanding equation (46) to the third order in $\sin\theta$. One obtains

$$|\kappa_x|\varepsilon S_t \geq \sin^2\theta + \kappa_x^2\left(1+(\varepsilon+1)^2\right)S_t^2. \tag{47}$$

To first order in Stokes, this criterion reduces to $|\kappa_x| \leq S_t\kappa_z^2\varepsilon$, as found in Section 3.1. Equation (46) shows that the unstable epicycle growth scales as S_t^2. Fig. 2 shows the imaginary part of the unstable epicycle obtained numerically from the complete dispersion relation $\mathcal{P}_8$. The agreement with the analytic expansion is almost perfect. In particular, the analytic stability criterion given by equation (47) is well satisfied. Remarkably, the growth of the epicycle can occur in a few 10^3 of orbital periods for $f_p \gtrsim 0.2$ and $S_t \gtrsim 0.01$, a relevant time-scale for planetesimal formation (see Fig. 3).

3.2.4 Epicycles versus secular mode

An indicator of the relative efficiency of the two unstable modes can be obtained by the following procedure. For each mode and a given value of f_p and S_t, one maximizes the growth rate with respect to κ_x and κ_z. The ratio of the values obtained for the two modes are then compared, keeping in mind that maxima are not reached for the same values of κ_x and κ_z a priori. For consistency with the shearing-box approximation and the expansion of Section 3.2, κ_x and κ_z are chosen in the range $\left[0.1; S_t^{-1}\right]$. Fig. 3 shows that the growth rate of the epicycle can be as large as the one of the secular mode, for a wide range of dust fractions and Stokes numbers relevant for planetesimal formation.

To interpret this result, one first finds approximations for the values of κ_x and κ_z that maximizes the growth rate of the epicycle

$$|\kappa_z| \simeq S_t^{-1}, \tag{48}$$

$$|\kappa_x| \simeq \frac{\varepsilon}{2\left(2+(\varepsilon+1)^2\right)}|\kappa_z|, \text{ if } f_p < f_g,$$

$$|\kappa_x| \simeq \frac{\varepsilon}{2\left(1+(\varepsilon+1)^2\right)}|\kappa_z|, \text{ if } f_p \geq f_g. \tag{49}$$

The above dependency in S_t^{-1} for κ_x was originally commented by Youdin & Goodman (2005) – their short-wavelength limit – but without mathematical justification. Similarly, for the secular mode, one obtains $\kappa_x \sim S_t^{-1/2}$ as Youdin & Goodman (2005). In particular, one can explain the ridge observed in Fig. 3 for the contour line corresponding to 10^0, i.e. similar growth rate for the two modes. On one hand, the secular mode becomes stable for $f_p = f_g = 0.5$. On the other hand, the secular mode approaches the marginal limit of equality in equation (45) for $S_t \gtrsim 3\,10^{-2}$ and $f_p \lesssim 0.5$. Indeed, $\kappa_x \sim S_t^{-1/2}$ and κ_z is bounded by the value 0.1. Importantly, the corrections of order 3 introduced in Section 3.2 are necessary to interpret the appearance of this ridge. Finally, the phase velocity of the fastest growing epicycle matches the radial drift velocity of the background in the limit $f_p \ll 1$ as found by Squire & Hopkins (2018).

4 RELEVANCE FOR PLANETESIMAL FORMATION

4.1 Viscous damping

As a rule of thumb, one can estimate the resilience of the unstable modes with respect to viscous damping by comparing the viscous time-scale and the typical time over which the instability develops. In dimensionless quantities, this condition yields $\Im(\omega)\tau_\nu \gtrsim 1$, where

$$\tau_\nu = \frac{4\pi^2}{\kappa^2}\frac{1}{\alpha}\frac{g_e^2}{\Omega_{K,0}^2 c_s^2} \sim \frac{4\pi^2}{\kappa^2}\frac{1}{\alpha}\left(\frac{H}{r_0}\right). \tag{50}$$

Instability resists viscosity when $\Im(\omega) \gtrsim \alpha\frac{\kappa^2}{4\pi^2}\left(\frac{r_0}{H}\right)$. For typical discs with $\alpha = 5\times10^{-4}$ and $H/r_0 = 0.1$, one gets $\Im(\omega) \gtrsim 10^{-4}\kappa^2$. For the secular mode, the validity of this condition has been discussed in several studies (e.g. Youdin & Goodman 2005; Auffinger & Laibe 2018). For $\alpha \gtrsim 10^{-5} - 10^{-4}$, the growth of the secular mode is damped.

More generally, the secular mode grows when $\kappa_x \gtrsim \kappa_z$, implying that the threshold for viscous damping is set by the value of κ_x. Moreover, the growth rate of the secular mode varies as

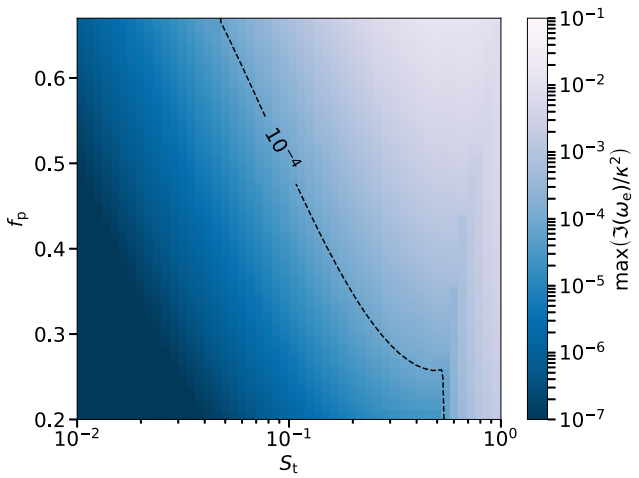

Figure 4. The maximum growth rate of the unstable epicycle normalized to κ^2. For a value α larger than 5 times the value indicated by the blue colour bar, the instability is damped by viscous dissipation. As an example, above the dashed black contour labelled 10^{-4}, the epicycle is unstable and resists the viscous damping associated with a value of $\alpha = 5 \times 10^{-4}$. Hence, epicycles can be more resilient against viscosity compared to the secular mode. Here, the aspect ratio is $H/r_0 = 0.1$.

$\sim \varepsilon \kappa_x^2 S_t^3 / \cos^2\theta$ (equation 42, see also Youdin & Goodman 2005; Jacquet et al. 2011). Large growth rates could be achieved with large values of κ_x. However, those modes are damped by viscosity. One finds that no secular mode can develop for $S_t \lesssim 0.01$. For values of S_t increasing from 0.01 to 0.1, only secular modes with reasonably small values of κ_x can develop and the associated time-scales go from $\sim 10^6$ to $\sim 10^3$ orbital periods. This regime becomes therefore relevant for planetesimal formation for $S_t \gtrsim 0.1$.

Fig. 4 shows similar analysis for the unstable epicycle in a disc where $\alpha = 5 \times 10^{-4}$ and $H/r_0 = 0.1$. From Section 3.2, one knows that epicycles become unstable for $\kappa_z \gg \kappa_x$. For this mode, the threshold for viscous damping is thus set by the value of κ_z. On the other hand, equation (46) shows that the growth rate of the epicycle varies as $\sim \epsilon^2 \kappa_x S_t^2$. Reasonably small values of κ_z and κ_x can therefore allow the instability to develop without being damped. This happens for $S_t \gtrsim 0.1$ and gives time-scales of $\sim 10^3$ orbital periods, which compares with the ones obtained for the secular mode. For both modes, much shorter growth time can be achieved for larger Stokes numbers (see Fig. 3). For classical T-Tauri star discs, streaming instability may therefore concentrate efficiently (sub)millimetre-in-size grains, relieving the constrain of the fragmentation barrier. As a final remark, Auffinger & Laibe (2018) have shown that around a pressure bump, streaming instability may favour epicycles with respect to the secular mode (in this case, for large amplitudes of the bump) and resists viscous damping. In this situation as well, epicycles cannot be neglected.

4.2 Green's function analysis

In real discs, power spectrum is expected to peak at the orbital frequency and to cascade down by turbulence to larger frequencies. Hence, power is essentially injected at frequencies close to one of the epicycles. To understand how a dusty disc responds to a local perturbation, we study the evolution of a perturbation (equations 25–30) to a monochromatic source, switched on at $\tau = 0$, of the form

$$\boldsymbol{S_8}(\tau, \chi, \zeta) = \Theta(\tau) \tilde{\boldsymbol{S_8}} e^{i(\kappa_x \chi + \kappa_z \zeta - \omega_f \tau)}. \tag{51}$$

ω_f denotes the real driving frequency of the source, $\Theta(\tau)$ the Heaviside step function, $\boldsymbol{S_8}(\tau, \chi, \zeta)$ the vector expression of the source, and $\tilde{\boldsymbol{S_8}}$ its Fourier decomposition. Both have eight components corresponding to the eight perturbed quantities $(\delta, \boldsymbol{u}, \Delta\boldsymbol{u}, h)$. With these notations, the system of perturbed equations writes

$$(\boldsymbol{\Pi}_7 \partial_\tau + \mathbf{M}_8(\kappa_x, \kappa_z))\, \boldsymbol{P} = \boldsymbol{S_8}(\tau, \chi, \zeta), \tag{52}$$

where $\boldsymbol{\Pi}_7 = \mathrm{Diag}(1, 1, 1, 1, 1, 1, 1, 0)$ and the matrix of perturbations $\mathbf{M}_8(\kappa_x, \kappa_z)$ are 8×8 matrices, and $\boldsymbol{P} = (\delta, \boldsymbol{u}, \Delta\boldsymbol{u}, h)$ is a vector with eight components. Using a Laplace-transform and applying the residue theorem (e.g. Morse & Feshbach 1953), one obtains

$$\tilde{\boldsymbol{P}}(\tau) = \Theta(\tau) \Bigg([-i\omega_f \boldsymbol{\Pi}_7 + \mathbf{M}_8(\kappa_x, \kappa_z)]^{-1}\, \tilde{\boldsymbol{S_8}} e^{-i\omega_f \tau} + \sum_{n=1}^{6} \frac{\mathrm{adj}\,\{-i\omega_n \boldsymbol{\Pi}_7 + \mathbf{M}_8(\kappa_x, \kappa_z)\}\, \tilde{\boldsymbol{S_8}}}{-i\partial_\omega \mathcal{P}_8(\omega_{\mathbb{R},n} + i s_n)} \frac{e^{(s_n \tau - i\omega_{\mathbb{R},n}\tau)}}{i(\omega_f - \omega_{\mathbb{R},n}) + s_n} \Bigg), \tag{53}$$

where $\boldsymbol{P}(\tau, \chi, \zeta) = \tilde{\boldsymbol{P}}(\tau) e^{i(\kappa_x \chi + \kappa_z \zeta)}$ is the response of the disc to the excitation, $\boldsymbol{S_8}(\tau, \chi, \zeta)$, $\omega_n = \omega_{\mathbb{R},n} + i s_n$ is the nth zero of the dispersion relation $\mathcal{P}_8(\omega) = 0$, and adj denotes the matrix adjugate. The form of equation (53) is generic. Similar responses have been extensively studied in the literature (e.g. Huerre & Monkewitz 1990; Lingwood 1997).

From equation (53), the perturbation can be decomposed in two parts: an oscillatory part with frequency ω_f (the first term of the right-hand side of equation 53) and a superposition of the six characteristic waves of the disc that may grow or be damped. Would all waves be damped, the asymptotic response at large times would reduce to the single usual oscillatory part of frequency ω_f. The interesting part for planetesimal formation is the transient regime described by the second term of the right-hand side of equation (53), which is dominated by growing modes. Streaming instability requires care, since two unstable modes with similar growth rates coexist (Section 4.1).

The source term $\boldsymbol{S_8}$ excites the waves with different amplitudes. Equation (53) shows that these amplitudes result from cumulative effects due to different factors. A first factor of spatial origin is the decomposition of the source term on to the eigenvectors of $\mathrm{adj}\,\{-i\omega_n \boldsymbol{\Pi}_7 + \mathbf{M}_8(\kappa_x, \kappa_z)\}$. In real discs, source terms are stochastic and should not favour any eigenmode in average. We expect therefore a similar mean contribution of this factor for both the epicycles and the secular mode. A second factor of temporal origin is the product $(i(\omega_f - \omega_{\mathbb{R},n}) + s_n)\partial_\omega \mathcal{P}_8(\omega_{\mathbb{R},n} + i s_n)$, which combines the distance of the driving frequency to the frequency of the unstable modes, and the ability of the disc to respond at the waves frequencies. Importantly, power is preferentially injected at frequencies ω_f close to the epicyclic frequencies. We therefore study the response to excitations such as $\omega_f \sim \omega_{\mathbb{R},e} \sim 1$.

We use the analytic expression for $\mathcal{P}_8^{(3)}$ derived in Section 3.2 to estimate the relative values of the factors $\partial_\omega \mathcal{P}_8(\omega_{e,s})$ that weigh the driven amplitudes a_e and a_s of the epicycles and the secular modes, respectively. The driving term $\boldsymbol{S_8}$ has been decomposed on to spatial Fourier mode in equation (51) and the driving frequency ω_f can be associated with several values of $\boldsymbol{\kappa}$, themselves associated with various epicycles and secular modes. For both modes, we obtain the relation $\partial_\omega \mathcal{P}_8(\omega_{e,s}) \sim \boldsymbol{\kappa}^2 \left(\cos^2\theta + \mathcal{O}(S_t)\right)$. Hence, the scalings $\partial_\omega \mathcal{P}_8(\omega_e) \sim \boldsymbol{\kappa}^2$ for unstable epicycles and $\partial_\omega \mathcal{P}_8(\omega_s) \sim \boldsymbol{\kappa}^2 S_t$ for the secular mode. Unstable epicycles should additionally satisfy $s_e \sim$

S_t^2 and $\sin\theta \lesssim S_t$ (Section 3.2). One gets

$$\mathrm{i}(\omega_f - \omega_{\mathbb{R},e}) + s_e \simeq s_e \sim S_t^2. \tag{54}$$

On the other hand, the secular mode satisfies

$$\mathrm{i}(\omega_f - \omega_{\mathbb{R},s}) + s_s \simeq \mathrm{i}\,\omega_f \sim 1. \tag{55}$$

Combining all these contributions gives a ratio

$$\frac{a_e}{a_s} \sim \frac{S_t^{-2}}{S_t^{-1}} \frac{\kappa_s^2}{\kappa_e^2}, \tag{56}$$

for the relative amplitudes of the epicycles and the secular mode. From Section 4.1, the values of κ_s^2 and κ_e^2 that ensure for the modes to resist viscous damping and to develop time-scales relevant for planetesimal formation are such that $\kappa_s^2/\kappa_e^2 \sim 1$. Hence, equation (56) reduces to

$$\frac{a_e}{a_s} \sim S_t^{-1} \gg 1. \tag{57}$$

We therefore expect that for pebbles with $S_t \ll 1$, streaming instability develops in discs essentially through the channel of its unstable epicycles. At later times, the secular mode will assist the growth, but non-linear effects may already be not negligible anymore.

5 CONCLUSION

In this study, we revisit the linear growth of the streaming instability in dusty discs. The dispersion relation that characterizes linear perturbations is analysed by the mean of a self-consistent expansion at third order with respect to the Stokes number. We provide an approximate dispersion relation that factorizes the two epicycles and the secular mode. Important terms that were neglected previously are subsequently integrated. The analytic approximation agrees almost perfectly with numerical results on the full system. Moreover, we use Green's function analysis to investigate the response of a disc to realistic excitations. From these derivations, we find that

(i) Contrary to what is often mentioned in the literature, the secular mode can be stable. We derive an accurate analytic criterion for its stability (equation 45).

(ii) Epicycles can also be unstable, whether the secular mode is stable or not. We derive its growth rates and its associated stability condition (equation 47).

(iii) Epicyclic modes can grow as fast as the secular modes. They can however be more resilient against viscous damping and be excited most efficiently in real discs (equation 57).

Streaming instability is known to be a privileged mechanism for planetesimal formation, but from the findings of this study, it may preferentially develop through the unexpected channel of unstable epicycles.

ACKNOWLEDGEMENTS

We acknowledge financial support from the national programs (PNP, PNPS, PCMI) of INSU, CNRS, CEA, and CNES, France. This project was partly supported by the IDEXLyon project (contract nANR-16-IDEX-0005) under the auspices University of Lyon. This project has received funding from the European Union's Horizon 2020 research and innovation programme under the Marie Skłodowska-Curie grant agreement No 823823. This work has received funding from the European Research Council (ERC) under the European Union's Horizon 2020 research and innovation programme (grant agreement ERC advanced grant 740021-ARTHUS, PI: Thomas Buchert). We thank the referee for his constructive report. We have used MATHEMATICA (Wolfram Research 14).

REFERENCES

ALMA Partnership, 2015, ApJ, 808, L3
Andrews S. M. et al., 2018, ApJ, 869, L41
Auffinger J., Laibe G., 2018, MNRAS, 473, 796
Avenhaus H. et al., 2018, ApJ, 863, 44
Bai X.-N., Stone J. M., 2010a, ApJS, 190, 297
Bai X.-N., Stone J. M., 2010b, ApJ, 722, 1437
Bai X.-N., Stone J. M., 2010c, ApJ, 722, L220
Balsara D. S., Tilley D. A., Rettig T., Brittain S. D., 2009, MNRAS, 397, 24
Benisty M. et al., 2015, A&A, 578, L6
Blum J., Wurm G., 2008, ARA&A, 46, 21
Carrera D., Gorti U., Johansen A., Davies M. B., 2017, ApJ, 839, 16
Chiang E., Youdin A. N., 2010, Annu. Rev. Earth Planet. Sci., 38, 493
Christiaens V., Cantalloube F., Casassus S., Price D. J., Absil O., Pinte C., Girard J., Montesinos M., 2019, ApJ, 877, L33
Debras F., Mayne N., Baraffe I., Jaupart E., Mourier P., Laibe G., Goffrey T., Thuburn J., 2020, A&A, 633, A2
Drążkowska J., Dullemond C. P., 2014, A&A, 572, A78
Goldreich P., Lynden-Bell D., 1965, MNRAS, 130, 125
Goodman J., Pindor B., 2000, Icarus, 148, 537
Hopkins P. F., Squire J., 2018, MNRAS, 479, 4681
Huerre P., Monkewitz P. A., 1990, Annu. Rev. Fluid Mech., 22, 473
Jacquet E., Balbus S., Latter H., 2011, MNRAS, 415, 3591
Johansen A., Youdin A., 2007, ApJ, 662, 627
Johansen A., Oishi J. S., Low M., Klahr H., Henning T., Youdin A., 2007, Nature, 448, 1022
Johansen A., Youdin A., Mac Low M.-M., 2009, ApJ, 704, L75
Johansen A., Youdin A. N., Lithwick Y., 2012, A&A, 537, A125
Keppler M. et al., 2018, A&A, 617, A44
Keppler M. et al., 2019, A&A, 625, A118
Kowalik K., Hanasz M., Wóltański D., Gawryszczak A., 2013, MNRAS, 434, 1460
Krapp L., Benítez-Llambay P., Gressel O., Pessah M. E., 2019, ApJ, 878, L30
Laibe G., Price D. J., 2014, MNRAS, 444, 1940
Lebreuilly U., Commerçon B., Laibe G., 2019, A&A, 626, A96
Lingwood R. J., 1997, Stud. Appl. Math., 98, 213
Lyra W., Kuchner M., 2013, Nature, 499, 184
Morse P. M., Feshbach H., 1953, Methods of Theoretical Physics, Part I. McGraw-Hill, New York, p. 791
Nakagawa Y., Sekiya M., Hayashi C., 1986, Icarus, 67, 375
Pinte C. et al., 2018, ApJ, 860, L13
Pinte C. et al., 2019, Nat. Astron., 3, 1109
Saffman P. G., 1962, J. Fluid Mech., 13, 120
Schäfer U., Yang C.-C., Johansen A., 2017, A&A, 597, A69
Schoonenberg D., Ormel C. W., 2017, A&A, 602, A21
Simon J. B., Armitage P. J., Li R., Youdin A. N., 2016, ApJ, 822, 55
Squire J., Hopkins P. F., 2018, ApJ, 856, L15
Teague R., Bae J., Bergin E. A., Birnstiel T., Foreman-Mackey D., 2018, ApJ, 860, L12
Testi L. et al., 2014, in Beuther H., Klessen R. S., Dullemond C. P., Henning T., eds, Protostars and Planets VI, Univ Arizona Press, Tucson Arizona, p. 339
Tilley D. A., Balsara D. S., Brittain S. D., Rettig T., 2010, MNRAS, 403, 211
van der Marel N. et al., 2013, Science, 340, 1199
Wolfram Research I, 14, Mathematica, Version 14.0, Available at: https://www.wolfram.com/mathematica
Yang C.-C., Johansen A., 2014, ApJ, 792, 86
Youdin A. N., Goodman J., 2005, ApJ, 620, 459
Youdin A., Johansen A., 2007, ApJ, 662, 613
Zhuravlev V. V., 2019, MNRAS, 489, 3850

APPENDIX A: DETERMINANT OF THE LINEAR SYSTEM $\mathcal{P}_8$

$$
\begin{vmatrix}
-\mathrm{i}\omega & \mathrm{i}\kappa_x & 0 & \mathrm{i}\kappa_z & 0 & 0 & 0 & 0 \\
\frac{\mathrm{i}\kappa_x S_\mathrm{t}^2}{\left(S_\mathrm{t}^2+1\right)^2}+1 & -\mathrm{i}\omega & -2 & 0 & -\frac{2\mathrm{i}f_\mathrm{p}\kappa_x S_\mathrm{t}}{S_\mathrm{t}^2+1} & 0 & -\frac{\mathrm{i}f_\mathrm{p}\kappa_z S_\mathrm{t}}{S_\mathrm{t}^2+1} & \mathrm{i}\kappa_x \\
-\frac{\mathrm{i}\kappa_x S_\mathrm{t}^3}{2\left(S_\mathrm{t}^2+1\right)^2} & \frac{1}{2} & -\mathrm{i}\omega & 0 & \frac{\mathrm{i}f_\mathrm{p}\kappa_x S_\mathrm{t}^2}{2\left(S_\mathrm{t}^2+1\right)} & -\frac{\mathrm{i}f_\mathrm{p}\kappa_x S_\mathrm{t}}{S_\mathrm{t}^2+1} & \frac{\mathrm{i}f_\mathrm{p}\kappa_z S_\mathrm{t}^2}{2\left(S_\mathrm{t}^2+1\right)} & 0 \\
0 & 0 & 0 & -\mathrm{i}\omega & 0 & 0 & -\frac{\mathrm{i}f_\mathrm{p}\kappa_x S_\mathrm{t}}{S_\mathrm{t}^2+1} & \mathrm{i}\kappa_z \\
\frac{\mathrm{i}\kappa_x S_\mathrm{t}^3}{f_\mathrm{g}\left(S_\mathrm{t}^2+1\right)^2}-\frac{S_\mathrm{t}}{f_\mathrm{g}\left(S_\mathrm{t}^2+1\right)} & -\frac{\mathrm{i}\kappa_x S_\mathrm{t}^2}{f_\mathrm{g}\left(S_\mathrm{t}^2+1\right)} & 0 & 0 & -\frac{\mathrm{i}(2f_\mathrm{p}-1)\kappa_x S_\mathrm{t}^2}{f_\mathrm{g}\left(S_\mathrm{t}^2+1\right)}-\mathrm{i}\omega S_\mathrm{t}+1 & -2S_\mathrm{t} & 0 & -\frac{\mathrm{i}\kappa_x S_\mathrm{t}}{f_\mathrm{g}} \\
\frac{S_\mathrm{t}^2}{2f_\mathrm{g}\left(S_\mathrm{t}^2+1\right)}-\frac{\mathrm{i}\kappa_x S_\mathrm{t}^4}{2f_\mathrm{g}\left(S_\mathrm{t}^2+1\right)^2} & 0 & -\frac{\mathrm{i}\kappa_x S_\mathrm{t}^2}{f_\mathrm{g}\left(S_\mathrm{t}^2+1\right)} & 0 & \frac{S_\mathrm{t}}{2} & -\frac{\mathrm{i}(2f_\mathrm{p}-1)\kappa_x S_\mathrm{t}^2}{f_\mathrm{g}\left(S_\mathrm{t}^2+1\right)}-\mathrm{i}\omega S_\mathrm{t}+1 & 0 & 0 \\
0 & 0 & 0 & -\frac{\mathrm{i}\kappa_x S_\mathrm{t}^2}{f_\mathrm{g}\left(S_\mathrm{t}^2+1\right)} & 0 & 0 & -\frac{\mathrm{i}(2f_\mathrm{p}-1)\kappa_x S_\mathrm{t}^2}{f_\mathrm{g}\left(S_\mathrm{t}^2+1\right)}-\mathrm{i}\omega S_\mathrm{t}+1 & -\frac{\mathrm{i}\kappa_z S_\mathrm{t}}{f_\mathrm{g}} \\
\frac{\kappa_x S_\mathrm{t}}{S_\mathrm{t}^2+1} & \kappa_x & 0 & \kappa_z & -f_\mathrm{p}\kappa_x & 0 & -f_\mathrm{p}\kappa_z & 0
\end{vmatrix}. \tag{A1}
$$

APPENDIX B: THIRD-ORDER POLYNOMIAL

$$
\begin{aligned}
\mathcal{P}_8^{(3)}(\omega) = {} & \mathrm{i}\frac{S_\mathrm{t}^3}{f_\mathrm{g}}\omega^6 - \frac{2+f_\mathrm{g}}{f_\mathrm{g}}S_\mathrm{t}^2\omega^5 \\
& + \left\{-\mathrm{i}\frac{1+2f_\mathrm{g}}{f_\mathrm{g}}S_\mathrm{t} + \frac{S_\mathrm{t}^3}{f_\mathrm{g}^2}\left(-\mathrm{i}f_\mathrm{g}\left(1+\cos^2\theta\right) - 2\kappa_x - 6f_\mathrm{g}\kappa_x + 11f_\mathrm{g}^2\kappa_x\right)\right\}\omega^4 \\
& + \left\{1 + \frac{S_\mathrm{t}^2}{f_\mathrm{g}}\left(2 + f_\mathrm{g}(3\cos^2\theta - 1) - 6\mathrm{i}\kappa_x f_\mathrm{p}\right)\right\}\omega^3 \\
& + \left\{\left(-\mathrm{i}(1-3\cos^2\theta) + \frac{\mathrm{i}}{f_\mathrm{g}} + \kappa_x\right)S_\mathrm{t} + \left(\kappa_x\left(5 - 15\cos^2\theta + \frac{2}{f_\mathrm{g}^2} - \frac{7}{f_\mathrm{g}} + \frac{12}{f_\mathrm{g}}\cos^2\theta + 4\mathrm{i}\kappa_x - \frac{\mathrm{i}\kappa_x}{f_\mathrm{g}}\right) + \frac{\mathrm{i}\cos^2\theta}{f_\mathrm{g}}\right)S_\mathrm{t}^3\right\}\omega^2 \\
& + \cos^2\theta\left\{-1 + S_\mathrm{t}^2\left(-1 + 3\mathrm{i}\kappa_x\left(\frac{1}{f_\mathrm{g}} - 1\right)\right)\right\}\omega \\
& + \kappa_x\cos^2\theta\left\{\left(-2 + \frac{1}{f_\mathrm{g}}\right)S_\mathrm{t} + \left(2 - \frac{2}{f_\mathrm{g}} - 12\mathrm{i}\kappa_x\left(1 - \frac{1}{f_\mathrm{g}}\right) - 3\mathrm{i}\frac{\kappa_x}{f_\mathrm{g}^2}\right)S_\mathrm{t}^3\right\}.
\end{aligned} \tag{B1}
$$

APPENDIX C: COEFFICIENTS OF THE EUCLIDIAN FACTORIZATION

$$
\begin{aligned}
\alpha_1 &= -\frac{f_\mathrm{p}}{2f_\mathrm{g}}\left(\kappa_x + \mathrm{i}\sin^2\theta\right), \\
\alpha_2 &= \frac{1}{2\cos\theta}\frac{f_\mathrm{p}}{f_\mathrm{g}^2}\left(\frac{f_\mathrm{p}\kappa_x^2}{4} - \frac{\sin^4\theta\, f_\mathrm{p}}{4} - (f_\mathrm{p} - f\mathrm{g})\kappa_x^2 + \cos^2\theta\sin^2\theta - \mathrm{i}\kappa_x\left(f_\mathrm{p} - \frac{\sin^2\theta}{2}(1+f_\mathrm{g})\right)\right), \\
\alpha_3 &= \frac{f_\mathrm{p}\kappa_x}{4f_\mathrm{g}^3}\left((1+f_\mathrm{g}(1+f_\mathrm{g})) - \left(1 - f_\mathrm{p}(1+f_\mathrm{p})\right)\cos(2\theta) - 2\frac{(f_\mathrm{p}-f_\mathrm{g})^2}{\cos^2\theta}\kappa_x^2\right) \\
&\quad - \frac{\mathrm{i}f_\mathrm{p}}{2f_\mathrm{g}^3}\left(f_\mathrm{p}(2+f_\mathrm{g})\sin^4\theta + f_\mathrm{g}(1+2f_\mathrm{p})\kappa_x^2 - \sin^2\theta + \frac{(f_\mathrm{p}-f_\mathrm{g})^2}{\cos^2\theta}\kappa_x^2\right), \\
\beta_0 &= -S_\mathrm{t}\frac{\kappa_x(f_\mathrm{p}-f_\mathrm{g})}{f_\mathrm{g}} + S_\mathrm{t}^3\left(-\kappa_x\left(-\frac{2f_\mathrm{p}}{f_\mathrm{g}} + \frac{12\mathrm{i}\kappa_x f_\mathrm{p}}{f_\mathrm{g}} - \frac{3\mathrm{i}\kappa_x}{f_\mathrm{g}^2}\right) + \frac{\kappa_x(f_\mathrm{p}-f_\mathrm{g})}{f_\mathrm{g}}\left(\frac{2\alpha_2}{\cos\theta} - \frac{\alpha_1^2}{\cos^2\theta}\right)\right), \\
\beta_1 &= 1 + \frac{S_\mathrm{t}^2}{f_\mathrm{g}}\left(f_\mathrm{g} - \frac{f_\mathrm{p}}{f_\mathrm{g}}\sin^2\theta - \mathrm{i}\frac{\kappa_x f_\mathrm{p}}{f_\mathrm{g}}\left(4f_\mathrm{g} - 1\right)\right), \\
\beta_2 &= -\mathrm{i}\frac{1+2f_\mathrm{g}}{f_\mathrm{g}}S_\mathrm{t} + \frac{S_\mathrm{t}^3}{f_\mathrm{g}^2}\left(-\mathrm{i}f_\mathrm{g} + \mathrm{i}f_\mathrm{p}\left(2+f_\mathrm{g}\right)\sin^2\theta\ -7f_\mathrm{p}f_\mathrm{g}\kappa_x + 3f_\mathrm{g}^2\kappa_x\right).
\end{aligned} \tag{C1}
$$

This paper has been typeset from a TEX/LATEX file prepared by the author.